In conjunction with the enhancement of societal living standards and the rapid development of information technology, an extensive variety of high-capacity electronic devices are being introduced to the market. The heightened demands result in the generation of electromagnetic wave radiation, which poses a potential risk to human well-being. Barium hexaferrite (BHF) is one of the radar-absorbing materials (RAMs) that can absorb electromagnetic waves because it has a high anisotropic field. However, its drawbacks are narrow absorption and less stability. Molybdenum disulfide (MoS_2), is the best candidate for the reinforcement of BHF. The study investigated the impact of increasing the thiourea, temperature, hydrothermal holding time, and sample thickness on reflection loss. This study used a two-step molten salt and hydrothermal synthesis to make a $BaFe_{12}O_{19}$@MoS_2 core-cell composite. Two-step molten salt and hydrothermal synthesis methods created single-phase $BaFe_{12}O_{19}$@MoS_2 core-cell composites that worked well. The results showed that adding MoS_2 to BHF changed BHF's magnetic properties from hard to soft. Increasing the hydrothermal temperature up to 220 °C effectively reduced the reflection loss of $BaFe_{12}O_{19}$@MoS_2. On a 2 mm thick sample containing 100 mmol thiourea, the study achieved an electromagnetic wave absorption of 99.97 % with a reflection loss of −35.41 dB (17.37 GHz). The results of this research can be applied to protect electronic devices vulnerable to signal interference from satellite radar systems at frequencies of 12–18 GHz

Keywords: barium hexaferrite, core-shell composite, hydrothermal, molybdenum disulfide, radar absorber material, reflection loss

UDC 061
DOI: 10.15587/1729-4061.2023.291064

DEVELOPMENT OF BARIUM HEXAFERRITE CORE–SHELL COMPOSITES AS HIGH-PERFORMANCE MICROWAVE ABSORPTION BY OPTIMIZING HYDROTHERMAL SYNTHESIS

Erlina Yustanti
Corresponding author
Doctor of Materials Science, Professor*, Head of the Laboratory
Nanomaterial and Process Technology Laboratory**
E-mail: erlina.yustanti@untirta.ac.id
Alfian Noviyanto
Doctor of Philosophy, Managing Director and Principal Investigator, Assistant Professor
Center of Excellence Advanced Materials
Nano Center Indonesia
Raya Puspiptek str., A-12, Setu, Indonesia, 15314
Department of Mechanical Engineering
Mercu Buana University
Jend. Meruya Selatan str., Kebun Jeruk, Jakarta Indonesia, 11650
Annisa Nur Fauziah
Bachelor of Engineering*
Bachtiar Lubis
Bachelor of Engineering*
Adhitya Trenggono
Master of Materials Science, Head of Department of Metallurgical Engineering*
Material Functional Laboratory**
Ahmad Taufiq
Professor, Doctor of Physics, Head of Department of Physics
Department of Physics
Universitas Negeri Malang
Semarang str., 5, Malang, Indonesia, 65145
*Department of Metallurgical Engineering**
**Sultan Ageng Tirtayasa University
Jenderal Sudirman str., 03, Cilegon, Banten, Indonesia, 42435

Received date 20.09.2023
Accepted date 08.12.2023
Published date 27.12.2023
How to Cite: *Yustanti, E., Noviyanto, A., Fauziah, A. N., Lubis, B., Trenggono, A., Taufiq, A. (2023). Development of barium hexaferrite core–shell composites as high-performance microwave absorption by optimizing hydrothermal synthesis. Eastern-European Journal of Enterprise Technologies, 6 (10 (126)), 30–42. doi: https://doi.org/10.15587/1729-4061.2023.291064*

1. Introduction

People are exposed to electromagnetic wave radiation from various sources, such as high-speed computers, cell phones, microwave ovens, radar, and satellite communication. The rapid development of wireless communication technology has been linked to a rise in public awareness regarding the dangers of electromagnetic pollution. The adverse effects of electromagnetic pollution on wireless devices, accurate instruments, and military safety make it imperative to promptly create high-performance radar-absorbing materials that absorb electromagnetic waves at wide frequencies. The study used key parameters to change the morphology of the $BaFe_{12}O_{19}$@MoS_2 core-shell composite using hydro-

Copyright © 2023, Authors. This is an open access article under the Creative Commons CC BY license

thermal synthesis to make it excellent at high-performance microwave absorption with the thinnest sample. However, the study focused on radar-absorbing materials at 12–18 GHz.

Barium hexaferrite (BHF) is a hard magnet with anisotropy, a high Curie temperature, a large magnetic field, good chemical stability, and low corrosion. Barium M-Hexaferrite (BaM), with its hexagonal crystal structure, is a permanent magnet with the potential to become a raw material for absorbing microwaves. These few decades have seen much research into M-type hexagonal ferrite because it has many uses. Barium hexaferrite is used in multiferroics, microwave absorbers, high-density magnetic recording media, telecommunications equipment, and magneto-optics [1]. Ferrite nanoparticles are essential in science and technology because they are adsorptive, magnetic, and catalytic. Nanoparticles have large surface areas, ferrite-based materials have good thermal stability and mechanical properties, and their chemical composition is easy to engineer. It can be controlled to improve their performance [2]. BaM is a ferromagnetic oxide with dielectric and magnetic properties often applied to RF (radio frequency) and microwaves. The use of BaM as a permanent magnet and magnetic recorder is in great demand, so research about this continues to be improved.

The researchers previously developed anti-radar material with a more than 2.5 mm thickness. The results were achieved through a complicated and inefficient preparation process, combining various synthesis methods and layered composite techniques to form a core@shel@shell structure. Therefore, the studies are devoted to creating the thinnest sample of radar absorber material with maximum electromagnetic wave absorption with efficient preparations are scientific relevance.

2. Literature review and problem statement

In a previous study conducted by [3], sol-gel auto-combustion confirmed the successful substitution of Er–Cr cations in the $SrEr_xCr_xFe_{12-2x}O_{19}$ achieved maximum reflection loss of −34.71 dB at x=0.5. However, this study does not explain the influence of the $SrEr_xCr_xFe_{12-2x}O_{19}$ morphological structure on the increased absorption of electromagnetic waves. Radar-absorbing materials can be created by producing barium hexaferrite from the top down or bottom up. High-power ultrasonic irradiation and mechanical alloying created $BaFe_9Mn_{1.5}Ti_{1.5}O_{19}$ with 90 % electromagnetic absorption and a reflection loss of −19.75 dB at 13.6 GHz [4]. Solid-state methods offer the benefits of waste-free production. However, important investigated morphological structure for over 90 % of electromagnetic wave absorption, which is unresolved in this paper. In addition, the paper [5] conducted an approach through a solid reaction that resulted in a reflection loss of −32.1 dB at 11.2 GHz. The study highlights the use of Co^{3+} at x=0.4 successfully synthesized using the thinnest sample, $BaFe_{12-x}Co_xO_{19}$. This research is superior in the x-band, but electromagnetic wave absorption is not optimal in the Ku band. Chemical vapour deposition with pyrolysis temperature control demonstrated that Fe@Fe_3C@CNTs ternary nanohybrids have significantly improved electromagnetic wave absorption capabilities [6]. The morphological samples were analyzed with variations in the pyrolysis temperature, while the hydrothermal process was conducted at 200 °C for 12 hours. This study did not examine the morphological impacts on temperature and hydrothermal holding time.

Previous researchers [7] successfully employed a hydrothermal synthesis technique to reduce reflection loss significantly to a remarkable value of −61 dB. This achievement was observed at a sample thickness of 1.7 mm. However, the influence of temperature and hydrothermal holding time has yet to be investigated. The production of $BaFe_{11.6}Mg_{0.2}Al_{0.2}O_{19}$ by a co-precipitation technique, employing a controlled calcination temperature of 900 °C, resulted in a reflection loss of −58.60 dB at a frequency of 10.91 GHz [8]. Due to the common usage of radar-absorbent material as a coating, this study did not conduct additional examination on differences in sample thickness. Therefore, it focused on samples with a thin thickness.

Several research studies have highlighted the significance of the mass ratio composition in determining the success of enhanced electromagnetic wave absorption. The practical synthesis of a multi-component composite using solvothermal fabrication was reported. The composite consisted of a core material, Fe_3O_4@C, and a shell material, MoS_2. It was shown that the microwave absorption behaviour of the composite could be easily modified by altering the mass ratio of the components [9]. The described multi-component composite technique demonstrates that raising the sample thickness from 2 to 3 mm increases reflection loss. These observations are interesting for further analysis since increased sample thickness generally leads to decreased reflection loss. As a result, developing a more uncomplicated encapsulating technique with comparable outcomes is interesting. Another researcher also reported based on electromagnetic characteristics, it was discovered that the Fe@Fe_3O_4 to MoS_2 mass ratio had a significant influence on the absorption and bandwidth [10]. Due to the increasing sample thickness, the reflection loss has shifted from the Ku band to the C band. Furthermore, additional improvements are needed to stabilize the increased sample thickness on the Ku Band by controlling the sample's morphology.

The researchers later developed a lot of layered composite techniques. Using double-layered absorbing structures proved to be a highly efficient method for enlarging absorption bandwidth. A sophisticated process that included hummers for RGO creation, hydrothermal fabrication, and hybrid structure production through co-precipitation produced MoS_2/RGO hybrids. Although MoS_2/RGO composites with increased microwave absorption properties have been reported [11]. However, this method use is limited due to the complicated and inefficient preparation process.

All this suggests that it is advisable to conduct a study investigating the influence of temperature and hydrothermal holding time, which researchers have yet to explore. The $BaFe_{12}O_{19}$@MoS_2 morphology also found an unresolved problem: the emergence of nanorod structures that block increased absorption of electromagnetic waves. Therefore, it is crucial to control the influence of several factors, such as hydrothermal temperature, holding time, thiourea composition, and sample thickness, to prevent the emergence of nanorods that inhibit the absorption of electromagnetic waves and enhance the absorption in the thinnest sample. This study developed a core-shell structure using a combination of molten salt and hydrothermal synthesis. This method is widely used in several industries due to its practicality, accessibility, cost-effectiveness, and efficiency compared to other methods.

3. The aim and objectives of the study

The study aims to develop techniques to improve the absorption of electromagnetic waves in barium hexaferrite with the thinnest sample. This will make it possible to apply

it as a coating material for electronic devices that require a thin anti-radar layer.

To achieve this aim, the following objectives are accomplished:

– to investigate the crystal structure of the $BaFe_{12}O_{19}$@MoS_2 core-shell composite;

– to investigate the morphology of the $BaFe_{12}O_{19}$@MoS_2 core-shell composite;

– to evaluate the magnetic properties of the $BaFe_{12}O_{19}$@MoS_2 core-shell composite;

– to investigate anti-radar capability.

4. Materials and methods

4. 1. Object and hypothesis of the study

The object of this study is to develop a technique for generating anti-radar material by using a coating material with the minimum possible sample thickness. The hypothesis proposes that by creating a core-shell composite, the crystal structure can be modified to enhance its ability to absorb electromagnetic waves. These modifications will reduce the adverse effects of electromagnetic waves on anti-radar material by minimizing their transmission and reflection. The premise underlying this work is that using MoS_2 as a dielectric material results in a significant decrease in reflection loss, hence optimizing the absorption of electromagnetic waves. The hydrothermal treatment's temperature and holding time significantly affect how well the core-shell composite is formed, especially when making the petals the right thickness and depth. This configuration facilitates a more concise core-shell synthesis, resulting in nearly 100 % absorption of electromagnetic waves.

The composition ratio of MoS_2:$BaFe_{12}O_{19}$ was changed in this study, along with the sample thickness, temperature, and holding time, during the hydrothermal synthesis process. The efficiency of reduced reflection loss in comparison to some of the synthesis factors was analyzed.

4. 2. Materials

Molten salt synthesis used a mixture of precursors: barium chloride dihydrate ($BaCl_2.2H_2O$, ≥99 %, Merck), iron (III) oxide (Fe_2O_3, ≥99 %, Sigma-Aldrich), barium carbonate ($BaCO_3$, ≥99 %, Pudak Scientific), and sodium chloride (NaCl, ≥99 %, Pudak Scientific). Hydrothermal synthesis used $BaFe_{12}O_{19}$ resulting from molten salt synthesis with thiourea (CH_4N_2S, ≥99 %, Loba Chemie), ammonium heptamolybdate tetrahydrate ($(NH_4)_6Mo_7O_{24}.4H_2O$, ≥99 %, Pudak Scientific), and deionized water from water-one.

4. 3. Synthesis of $BaFe_{12}O_{19}$@MoS_2 core-shell composite

In this study, two steps of molten salt synthesis and then hydrothermal synthesis were responsible for controlling the structure of the $BaFe_{12}O_{19}$@MoS_2 core-cell composite. The first step in making molten salt involved mixing $BaCO_3$, Fe_2O_3, and NaCl in a 1:2 mass ratio for $BaFe_{12}O_{19}$:NaCl. The precursors were milled using an alcohol medium at a speed of 150 rpm for 2 h, and then the wet milling product was calcined at 1000 °C for 2 h. In the second molten salt, there was a mixture of precursors of Fe_2O_3 and $BaCl_2.2H_2O$ with a mass ratio of 1:2 and $BaFe_{12}O_{19}$:Fe_2O_3 with a molar ratio of 1:500. The precursor mixture was milled at 150 rpm for 2 h. The sample was calcined at a temperature of 1100 °C for 8 h. In the synthesis of the $BaFe_{12}O_{19}$@MoS_2 core-shell composite, there was a mixture of 1 mmol $(NH_4)_6Mo_7O_{24}.4H_2O$, thiourea with a variation of (10, 20, 50, and 100) mmol, 35 ml deionized water, and 0.2 gr BHF. Then, the mixture was brought to the hydrothermal process at various temperatures (160, 180, 200, and 220) °C and holding times (14, 16, 18, and 20) h. A schematic illustration of the molten salt and hydrothermal synthesis of $BaFe_{12}O_{19}$@MoS_2 core-cell composite is shown in Fig. 1.

Table 1 lists all the codes used to identify the samples from the hydrothermal synthesis processes.

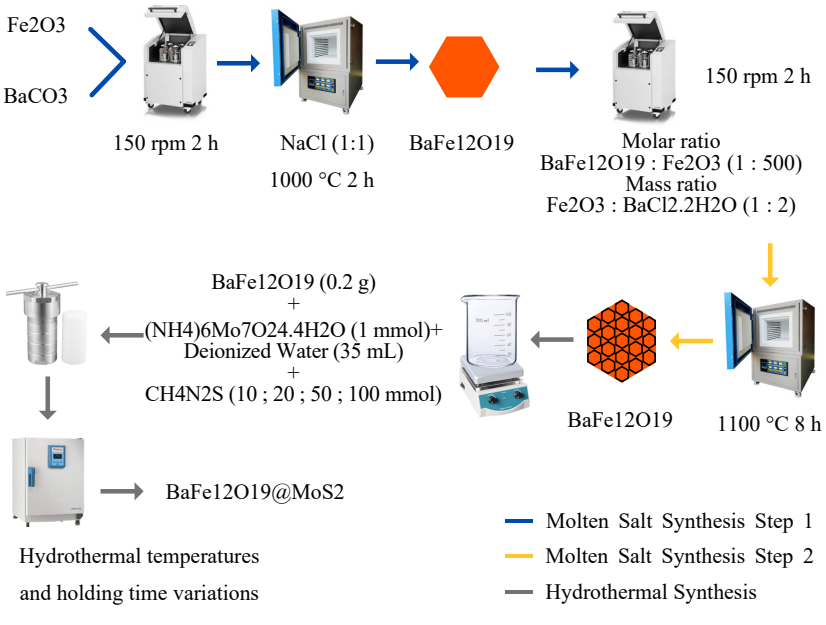

Fig. 1. Schematic of $BaFe_{12}O_{19}$ core-shell composite fabrication

Table 1

Code identification and treatment for all samples

Sample code	Thiourea composition at $BaFe_{12}O_{19}$@MoS_2 (mmol)	Sample thickness (mm)	Hydrothermal temperature (°C)	Hydrothermal holding time (h)
$BaFe_{12}O_{19}$	–	2	–	–
MoS_2	30	2	220	18
C_1	10	2	220	18
C_2	20	2	220	18
C_5	50	2	220	18
$C_{10}/T_{22}/H_{18}$	100	1.0; 1.5; 2.0; 2.5	220	18
T_{16}	100	2	160	18
T_{18}	100	2	180	18
T_{20}	100	2	200	18
H_{14}	100	2	220	14
H_{16}	100	2	220	16
H_{20}	100	2	220	20

C is the sample code $BaFe_{12}O_{19}$@MoS_2 with a composition variation of thiourea.

T is the sample code $BaFe_{12}O_{19}$@MoS_2 with hydrothermal temperature variations.

H is the sample code $BaFe_{12}O_{19}$@MoS_2 with hydrothermal holding time variation.

As for variation in sample thickness in representative sample code $C_{10}/H_{22}/T_{18}$.

4. 4. Characterization of the $BaFe_{12}O_{19}$@MoS_2 core-shell composite

The crystal structure was evaluated using x-ray diffraction (XRD, Bruker D8 Advance ECO with Lynxeye XE-T Cu Source) and scanning electron microscopy-energy dispersive x-ray spectroscopy (SEM-EDS, Carl Zeiss EVO 10) to determine the composition and morphology of the samples. Particle size distribution was analyzed using a particle size analyzer (PSA, Malvern Zetasizer Pro Blue Dynamic Light Scattering Instrument). Hysteresis loop analysis used a vibrating sample magnetometer (VSM, 1.2H, Oxford). The radar-absorbing materials (RAMs) performance was analyzed using a vector network analyzer (VNA, two ports, Anritsu MS 46322 A, Allen, TX, USA). The absorption power of EM waves was calculated based on reflection loss through the data generated by the transmission signal (S21) and the reflection signal (S11). The reflection loss (RL) was calculated using the equations of Nicholson Ross Weir [12–19] shown in equations (1) and (2):

$$Z_{in} = Z_0 \sqrt{\frac{\mu_r}{\varepsilon_r}} \tanh\left[j\left(\frac{2\pi f d}{c}\right)\sqrt{\mu_r \varepsilon_r}\right], \quad (1)$$

$$RL(\mathrm{dB}) = 20\log\left|\frac{Z_{in} - Z_0}{Z_{in} + Z_0}\right|. \quad (2)$$

The values ε and μ represent the relative permittivity and permeability, velocity of light in vacuum (c), electromagnetic frequency (f), sample thickness (d), impedance material (Z_{in}), and free space impedance (Z_0).

5. Experimental results of synthesizing $BaFe_{12}O_{19}$@MoS_2 core-shell composite

5. 1. Crystal structure of the $BaFe_{12}O_{19}$@MoS_2 core-shell composite

Fig. 2 compares the diffraction patterns of $BaFe_{12}O_{19}$, MoS_2, and $BaFe_{12}O_{19}$@MoS_2 core-shell composite.

Fig. 2 shows how the diffraction patterns of $BaFe_{12}O_{19}$ and MoS_2 in the standard database matched those of samples made of $BaFe_{12}O_{19}$, MoS_2, and a core-shell composite of $BaFe_{12}O_{19}$@MoS_2. Fig. 2 shows that $BaFe_{12}O_{19}$, MoS_2, and the $BaFe_{12}O_{19}$@MoS_2 core-shell composite have a single phase. The Crystallography Open Database (COD) number for $BaFe_{12}O_{19}$ is 1008841, and the COD number for MoS_2 is 1010993. Table 2 shows the results of the Rietveld refinement of $BaFe_{12}O_{19}$, MoS_2, $BaFe_{12}O_{19}$@MoS_2 (C_{10}), which has a hexagonal crystal structure. $BaFe_{12}O_{19}$@MoS_2 has space group P63/mmc, a=5.8924 Å, and b=23.1989 Å, which are the same as the results of a previous study [20].

Table 2

Rietveld refinement of $BaFe_{12}O_{19}$, MoS_2, and $BaFe_{12}O_{19}$@MoS_2 core-shell composite

Sample	$BaFe_{12}O_{19}$	MoS_2	$BaFe_{12}O_{19}$@MoS_2 (C_{10})
SIG	0.2315	0.62803	1.2952
Rwp (%)	17.9527	2.2720	6.6653
Rexp (%)	13.1957	12.2124	5.1761
a (Å)	5.8948	3.1439	5.8924
c (Å)	23.2129	12.3151	23.1989
Volume of unit cell (Å^3)	697.1736	107.708	697.5686
Density (g/cm^3)	5.2841	4.8800	5.2900

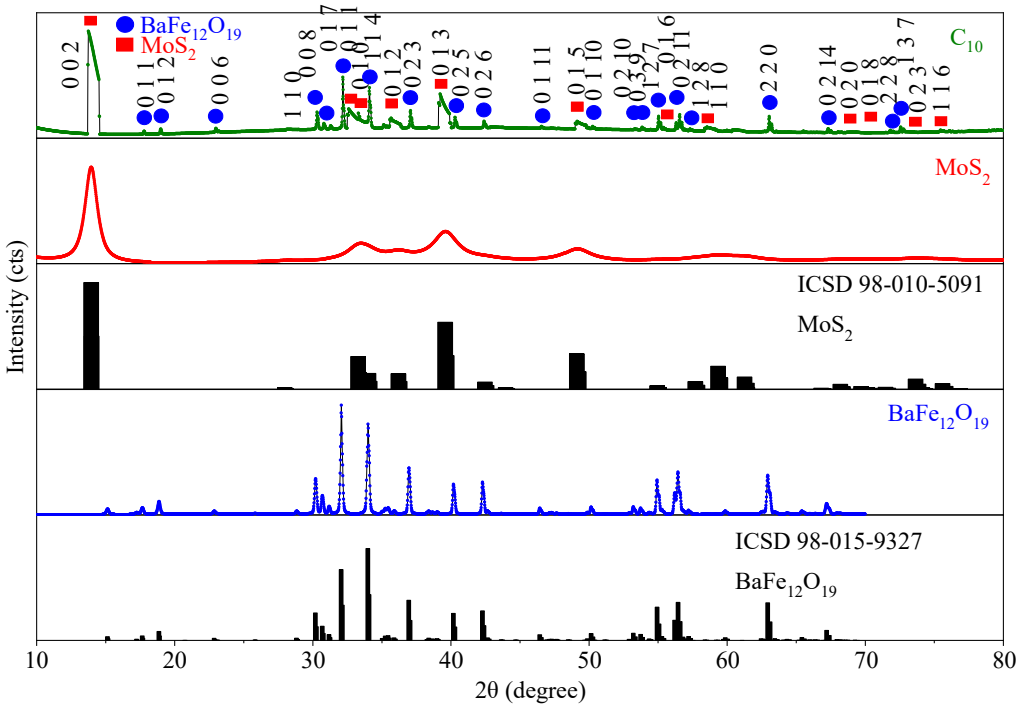

Fig. 2. The diffraction patterns of $BaFe_{12}O_{19}$, MoS_2, and $BaFe_{12}O_{19}$@MoS_2 core-shell composite

Table 2 shows the density of $BaFe_{12}O_{19}$ of 5.29 g/cm^3 is in line with the results of a previous study [21]. Furthermore, MoS_2 (space group=P63/mmc, a=3.1439 Å, c=12.3151 Å) is consistent with a previous study [22].

5. 2. The morphology of the $BaFe_{12}O_{19}$@MoS_2 core-shell composite

The surface morphology of the samples and the elemental composition of these materials were identified using SEM-EDS. Fig. 3 shows the EDS mapping to determine the composition and distribution of elements in the $BaFe_{12}O_{19}$@MoS_2 core-shell composite (C_{10}) has a homogeneous distribution.

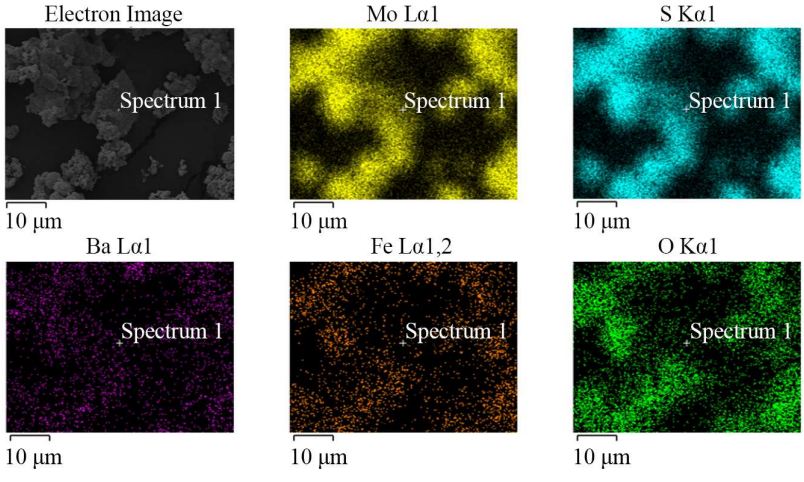

Fig. 3. The energy dispersive x-ray spectroscopy mapping of the $BaFe_{12}O_{19}$@MoS_2 (C_{10}) core-shell composite

As seen in Fig. 4 Spectrum 1, the detailed intensity of the $BaFe_{12}O_{19}$@MoS_2 (C_{10}) elemental composition.

Including the Au element within the $BaFe_{12}O_{19}$@MoS_2 (C_{10}) structure is feasible due to using Au as a coating during the sample preparation process. In order to achieve optimal imaging for non-conductive materials, it is typically necessary to use gold and carbon as coating elements. Table 3 summarizes the composition expressed in weight percentage (wt. %) and atomic percentage (at %) as depicted in Spectrum 1 of Fig. 4.

Fig. 5 shows the results of SEM characterization at 30,000 and 60,000 times magnification. Based on Fig. 5, *a* the structure morphology of the single-phase $BaFe_{12}O_{19}$ is a hexagonal plate-like crystal structure. Then, Fig. 5, *b* shows the single-phase nanoflower MoS_2, while Fig. 5, *c*–*f* shows the $BaFe_{12}O_{19}$@MoS_2 composites (C_1–C_{10}).

The results of the particle size distribution analysis performed with ImageJ software are summarized in Fig. 6. An increase in the thiourea composition of the $BaFe_{12}O_{19}$@MoS_2 core-shell composite increases the particle size. Based on the surface morphology of $BaFe_{12}O_{19}$@MoS_2, an increase in thiourea composition causes more MoS_2 to cover the surface of BHF. It was confirmed that the thiourea content was higher, which led to more agglomeration and MoS_2 growth on the surface of $BaFe_{12}O_{19}$. According to a previous study [7], when the amount of thiourea goes up, the growth pathway for MoS_2 nanoflowers on the BHF surface also gets longer and denser. According to Fig. 5, *f*, $BasFe_{12}O_{19}$@MoS_2 (C_{10}) has a distinctive morphology different from the other products containing the other thiourea compositions. The geometry of the nanoflower, which was suggested and made, could make it possible to get both a large contact area for intense interfacial polarization and a more significant number of places where electromagnetic waves could reflect and scatter [16]. An increasing concentration of thiourea increases the thickness of MoS_2, enhancing its ability to absorb electromagnetic waves on the BHF surface. Fig. 5, *f* demonstrates the maximum identified thickness and density of MoS_2 for the C_{10}.

Table 3

The element mapping of the $BaFe_{12}O_{19}$@MoS_2 core-shell composite (C_{10})

Element	Line type	Wt. %	Wt. % sigma	at %
O	K series	10.89	0.43	25.58
S	K series	35.55	0.83	48.37
Fe	L series	7.82	1.00	6.57
Mo	L series	42.34	1.04	16.08
Ba	L series	3.40	0.41	3.40

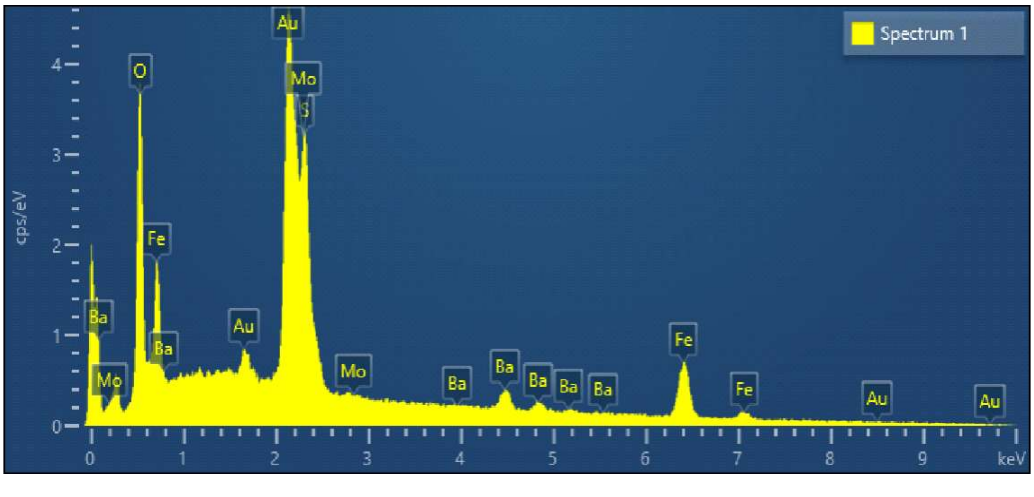

Fig. 4. The elemental content of the $BaFe_{12}O_{19}$@MoS_2 core-shell composite (C_{10})

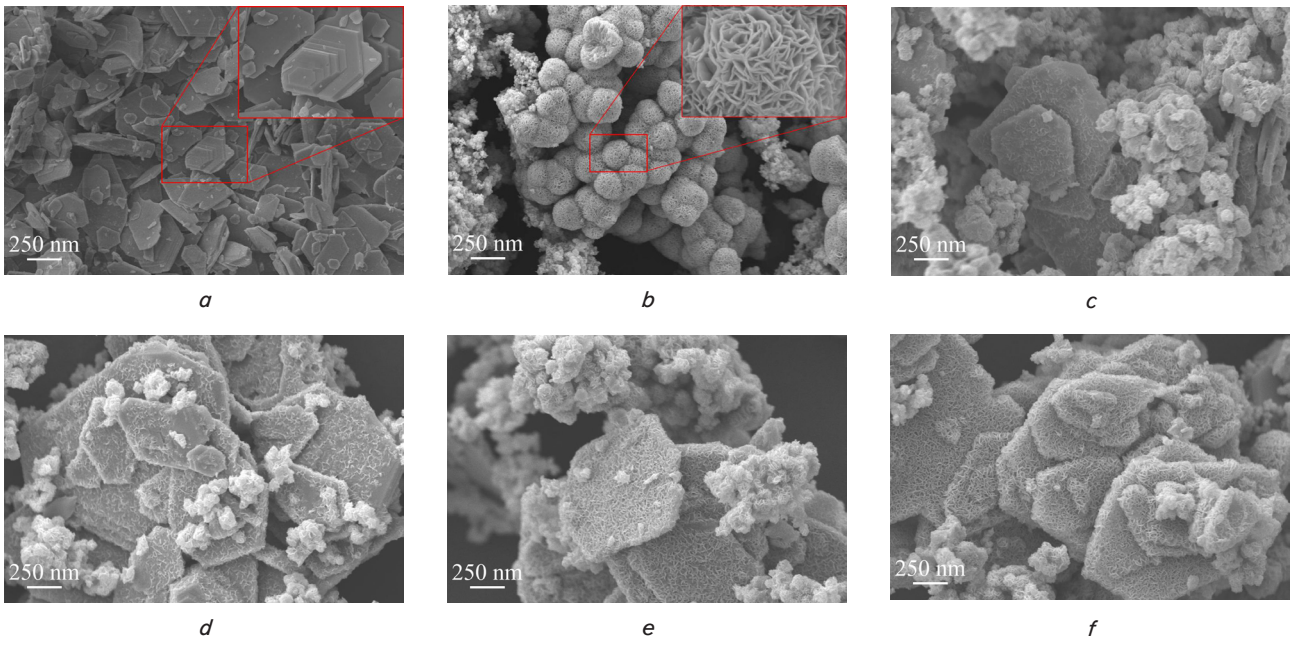

Fig. 5. The micrograph of particles size: *a* – $BaFe_{12}O_{19}$; *b* – MoS_2; *c*–*f* – $BaFe_{12}O_{19}$@MoS_2 (C_1–C_{10})

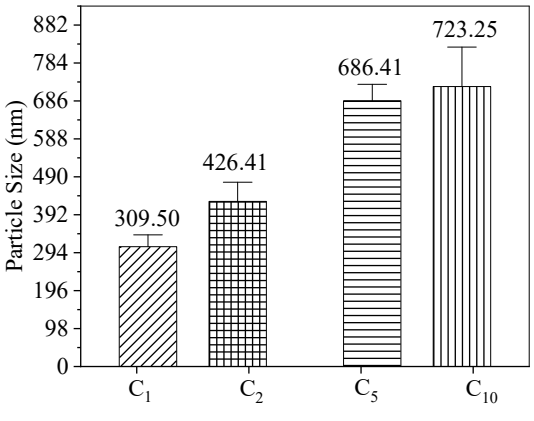

Fig. 6. The particle size of $BaFe_{12}O_{19}$@MoS_2 core-shell composite by using ImageJ analysis

The findings of SEM analysis of $BaFe_{12}O_{19}$@MoS_2 (C_{10}) to study the effect of temperature and hydrothermal holding time variations on the production of MoS_2 nanoflowers on the BHF surface are shown in Fig. 7. The particle size of the $BaFe_{12}O_{19}$@MoS_2 core-shell composite grows as the hydrothermal temperature rises (Fig. 7, *a*–*d*). As the hydrothermal holding time goes up, on the other hand, the nanoflower pathways on the surface of BHF tend to get bigger. The MoS_2 nanoflower petals also get denser, thicker, and more profound.

Fig. 7 illustrates the impact of elevated hydrothermal temperature on the morphology of a core-shell composite consisting of $BaFe_{12}O_{19}$@MoS_2. The process of MoS_2 nanorod creation initiates at a temperature of 160 °C, as depicted in Fig. 7, *b*. Subsequently, the temperature is raised to 180 °C and ultimately reaches its maximum at 200 °C. At a hydrothermal temperature of 220°C, a hexagonal $BaFe_{12}O_{19}$@MoS_2 floral structure may be observed (Fig. 7, *a*). The presence of the nanorod structure during synthesis is considered disadvantageous due to its disruptive effect on the electromagnetic wave absorption process. The presented figure illustrates the morphology of the sample free of nanorods when subjected to a hydrothermal temperature of 220 °C. Based on a previous study [13], nanowires were formed from nanorods at a temperature of 200 °C using hydrothermal synthesis. Decreasing the hydrothermal temperature increases the unwanted growth of MoS_2 nanorods. $BaFe_{12}O_{19}$@MoS_2 core-shell composite synthesis at a low temperature of 180 °C produces MoS_2 with nanorods and nanotube structures [23].

An analysis of particle size distribution was conducted using PSA. Brownian motion is the fundamental concept of PSA; when a group of particles scatters light, the scattering angle will be inversely proportional to the size of the particles. The crystallites' size and the sample's morphological structure depend on the precursor's composition, the solution's pH, and the temperature [24]. The particle size of the $BaFe_{12}O_{19}$@MoS_2 core-shell composite increases with increasing thiourea composition, as seen in Fig. 8. The ImageJ analysis results of SEM and PSA characterizations are reported in Table 4.

The particle size determined using PSA characterization, as shown in Table 4, follows the same trends and is not significantly different from the particle size determined using SEM, as shown in Fig. 6. Table 4 shows the PSA measurement findings, which demonstrate a polydispersity index (PI) in the range of 0.3–0.7. It demonstrates that the $BaFe_{12}O_{19}$@MoS_2 core-shell composite exhibits non-uniform particle sizes, various shapes, and a broad particle distribution; samples C_1 and C_5 even have bimodal curves.

Table 4

Particle size of $BaFe_{12}O_{19}$, MoS_2, and $BaFe_{12}O_{19}$@MoS_2 core-shell composite based on SEM and PSA analysis

Sample	SEM (nm)	PSA (nm)	Polydisperse index
$BaFe_{12}O_{19}$	485.6	410	0.4
MoS_2	345.6	287	0.4
C_1	309.50	356	0.6
C_2	426.41	415	0.3
C_5	686.41	660	0.7
C_{10}	723.25	847	0.7

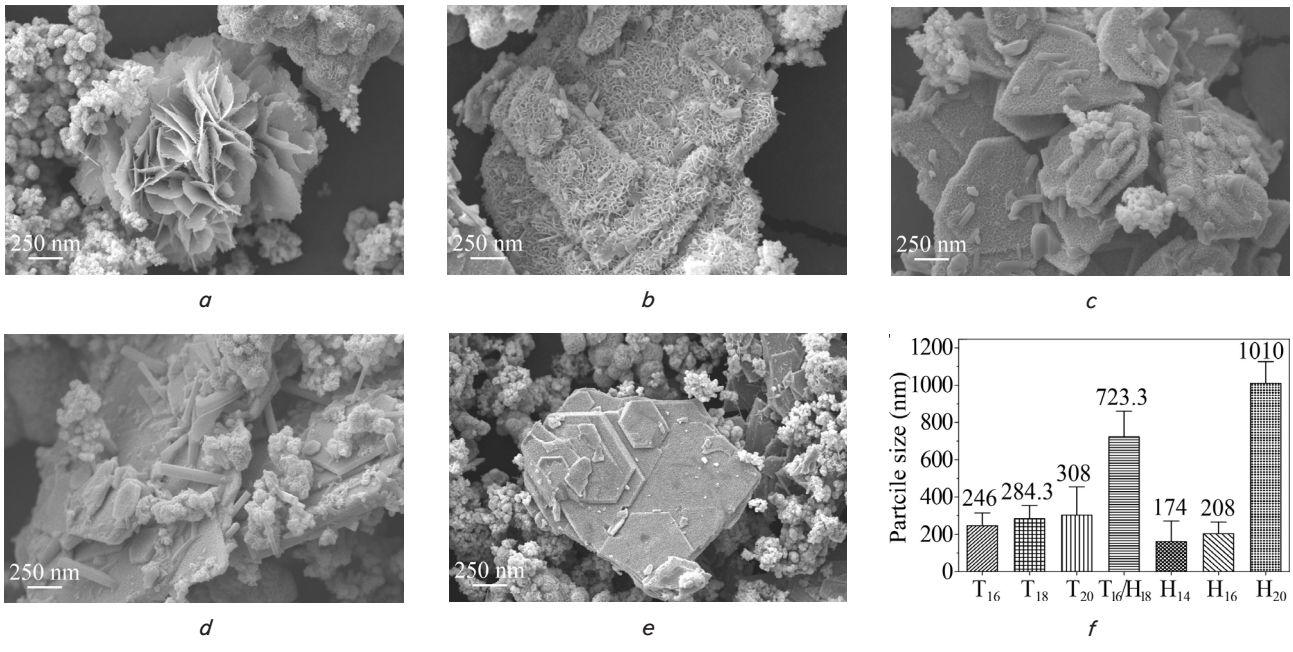

Fig. 7. The morphology of $BaFe_{12}O_{19}$@MoS_2: *a* – samples of $C_{10}/T_{22}/H_{18}$; *b–d* – hydrothermal temperatures of T_{16}, T_{18}, and T_{20}; *e–g* – hydrothermal holding times of H_{14}, H_{16}, and H_{20} *h* – histogram of particle size distribution

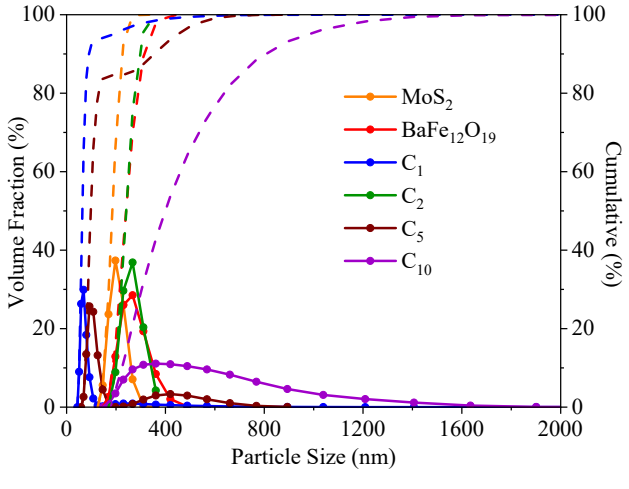

Fig. 8. Particle size distribution of the $BaFe_{12}O_{19}$, MoS_2, $BaFe_{12}O_{19}$@MoS_2

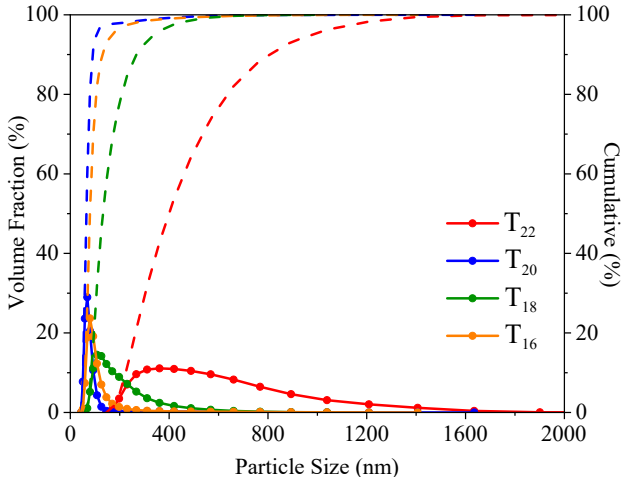

Fig. 9. Particle size distribution of $BaFe_{12}O_{19}$@MoS_2 core-shell composite at various hydrothermal temperatures

Fig. 9 shows that the increase in hydrothermal temperature is directly related to the increase in particle size and the widening of the particle size distribution of the $BaFe_{12}O_{19}$@MoS_2 core-shell composite. An increase in hydrothermal temperature from 160°C to 220 °C increases the *z*-average particle size from 257.5 nm to 847 nm.

Particle size growth is affected by the nucleation of the $BaFe_{12}O_{19}$@MoS_2 core-shell composite, which becomes more numerous when the hydrothermal temperature increases; this is also confirmed by a previous study [25, 26].

The influence of different hydrothermal holding durations on the particle size distribution of the $BaFe_{12}O_{19}$@MoS_2 core-shell composite is shown in Fig. 10.

The increase in the nucleation rate of the $BaFe_{12}O_{19}$@MoS_2 core-shell composite and the increase in hydrothermal holding time can increase the z-average from 174.2 nm to 993 nm. The increase in hydrothermal holding time is directly proportional to the increase in the size of the MoS_2 nanoflower; this is following a previous study [26].

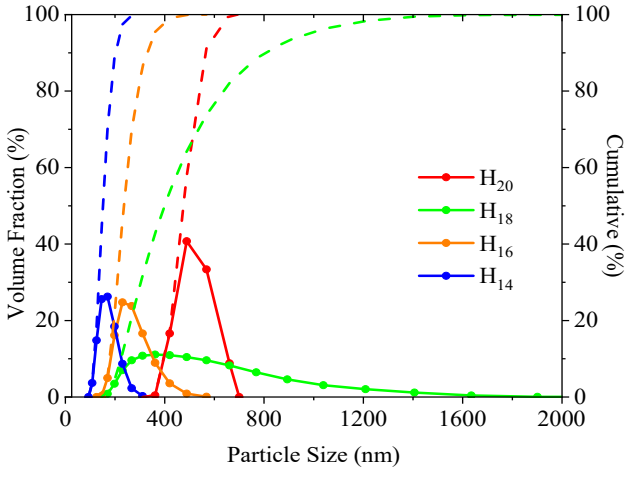

Fig. 10. Particle size distribution of $BaFe_{12}O_{19}$@MoS_2 core-shell composite at various hydrothermal holding times

Table 5 presents the particle sizes of $BaFe_{12}O_{19}$, MoS_2, and $BaFe_{12}O_{19}$@MoS_2 core-shell composites under different hydrothermal temperatures and holding times. This table compares the particle sizes obtained using scanning electron microscopy (SEM) and particle size analyzer (PSA) techniques.

Table 5

Particle sizes of the $BaFe_{12}O_{19}$@MoS_2 core-shell composites at various hydrothermal temperatures and holding times

Sample	SEM (nm)	PSA (nm)	Polydisperse index
T_{16}	246	257.5	0.4
T_{18}	284.3	284.3	0.6
T_{20}	308	308.1	0.4
T_{22}/H_{18}	723.3	847	0.7
H_{14}	174	174.2	0.3
H_{16}	208	284.2	0.3
H_{20}	1010	993	0.7

Table 5 compares the particle sizes obtained using scanning electron microscopy (SEM) and particle size analysis (PSA) techniques.

5. 3. The magnetic properties of the $BaFe_{12}O_{19}$@MoS_2 core-shell composite

The objective of employing a vibrating sample magnetometer is to analyze and determine the magnetic characteristics of $BaFe_{12}O_{19}$ and $BaFe_{12}O_{19}$@MoS_2, as illustrated in Fig. 11.

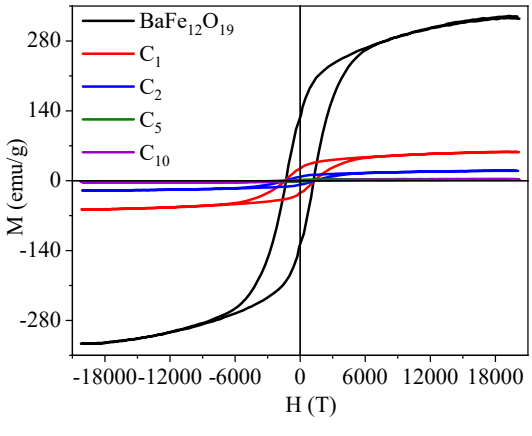

Fig. 11. Loop hysteresis of the $BaFe_{12}O_{19}$ and $BaFe_{12}O_{19}$@MoS_2 core-shell composites at various thiourea compositions

Fig. 11 shows that $BaFe_{12}O_{19}$ has the greatest magnetic saturation and remanence. Increasing thiourea composition (C_1–C_{10}) significantly decreases magnetic saturation and remanence. A decrease in magnetic saturation, remanence, and coercivity shows that $BaFe_{12}O_{19}$@MoS_2's properties change from those of a hard magnet to those of a soft magnet.

5. 4. Analysis of radar absorber performance using a vector network analyzer

A vector network analyzer (VNA) is used to prove the absorption performance of RAMs. VNA characterization results in the permeability and permittivity of real and imaginary. Real permeability and real permittivity represent the storage of electric and magnetic energy, while imaginary permeability and imaginary permittivity represent dielectric losses and magnetic losses in the sample [27]. Radar-absorbing material performance is calculated using reflection loss equations (1) and (2). Fig. 12 shows the reflection loss (RL) of $BaFe_{12}O_{19}$, MoS_2, and $BaFe_{12}O_{19}$@MoS_2 (C_1–C_{10}) at various thiourea compositions at a sample thickness of 2 mm.

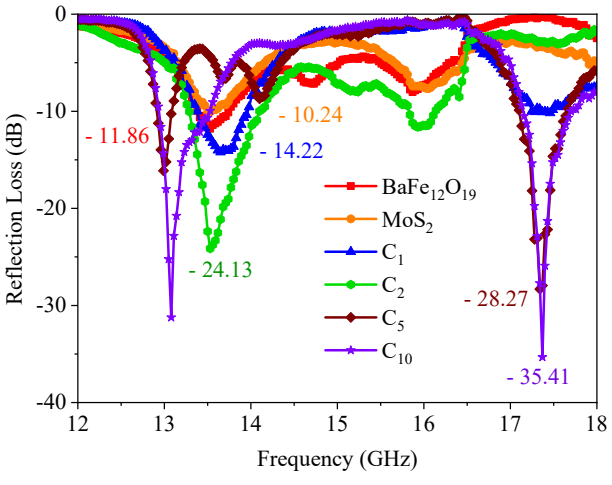

Fig. 12. Reflection loss of the $BaFe_{12}O_{19}$, MoS_2, $BaFe_{12}O_{19}$@MoS_2 core-shell composites at various thiourea compositions

Increasing thiourea composition reduces the RL of $BaFe_{12}O_{19}$@MoS_2 as much as 149.01 %, which is from –14.22 dB (13.65 GHz) to –35.41 dB (17.37 GHz). The $BaFe_{12}O_{19}$@MoS_2 (C_{10}) sample has a reflection loss of –35.41 dB (17.37 GHz) and an absorption rate of 99.97 %. The increase in thiourea on the $BaFe_{12}O_{19}$@MoS_2 core-shell composite shows that the entire surface of the barium hexaferrite is perfectly covered with MoS_2 nanoflowers. This research aligns with a previous study [7]. The increase in MoS_2 nanoflower growth is highly validated and matches the SEM morphological results in Fig. 5, *f*.

Fig. 13 shows that an increase in hydrothermal temperature reduces the reflection loss, namely 228.47 %, from –10.78 dB (17.37 GHz) to –35.41 dB (17.37 GHz).

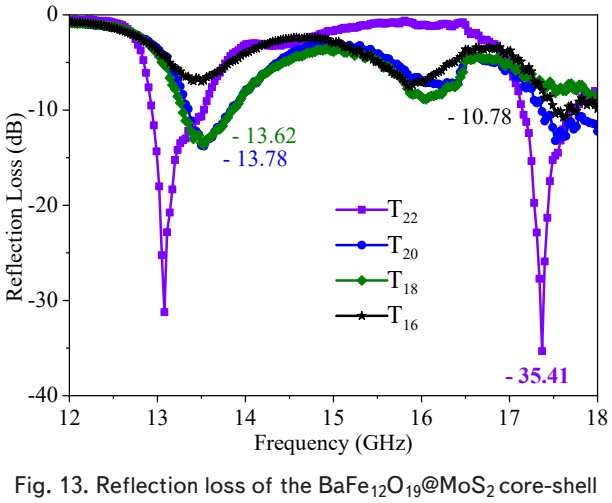

Fig. 13. Reflection loss of the $BaFe_{12}O_{19}$@MoS_2 core-shell composites at various hydrothermal temperatures

Controlling the hydrothermal temperature will affect the structure and morphology of the $BaFe_{12}O_{19}$@MoS_2 core-shell composite. In this research, the hydrothermal synthesis has the lowest RL and thickness at 220 °C. The precursors get enough Gibbs free energy to separate into larger particles. These findings are consistent with prior studies [28]

that have often seen an increase in temperature leading to the expansion of particle size.

Fig. 14 shows that as the hydrothermal holding time increases, the reflection loss decreases by 58 %, from −22.41 dB (13.53 GHz) to −35.41 dB (17.37 GHz).

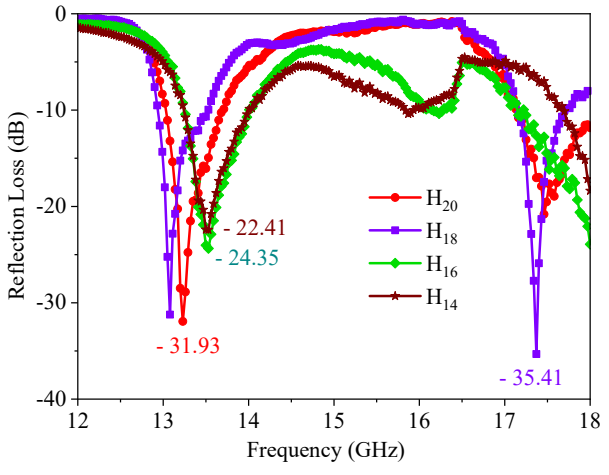

Fig. 14. Reflection loss of the $BaFe_{12}O_{19}$@MoS_2 core-shell composite at various hydrothermal holding times

Based on Fig. 10, the results of the PSA analysis prove that an increase in hydrothermal holding time causes an increase in particle size. Meanwhile, the SEM analysis results in Fig. 7 show that the increase in hydrothermal holding time affects the morphology and particle size of the $BaFe_{12}O_{19}$@MoS_2 core-shell composite. According to a previous study [28, 29], increasing the hydrothermal holding time changes how stable the nucleation of oxide powders is and makes the nucleation happen more, which makes the particles bigger.

A previous study [30] reported that increasing the sample thickness of RAMs decreases overall reflection loss. Increasing the sample thickness of the $BaFe_{12}O_{19}$@MoS_2 core-shell composite reduces reflection loss by 69.79 %, as shown in Fig. 15. When the sample has a thickness of 2.5 mm, it has been shown that up to 99.97 % of electromagnetic waves (EM) are absorbed. Additionally, at a frequency of 17.19 GHz, the reflection loss is measured at −35.48 dB. In this study, the thinnest sample thickness of 2 mm achieved a reflection loss of −35.41 dB (at a frequency of 17.37 GHz), resulting in an EM wave absorption rate of 99.97 %, the most attractive outcome.

These findings are consistent with prior studies [31] that have often seen an increase in temperature leading to the expansion of particle size. As shown in Fig. 15, increasing sample thickness improves electromagnetic wave absorption.

Table 6 shows $BaFe_{12}O_{19}$@MoS_2 synthesis achieving the lowest reflection at the thinnest sample thickness. It indicates that the purpose of this research is achieved.

Fig. 16 illustrates the growth mechanism of MoS_2 nanoflowers on $BaFe_{12}O_{19}$ during the synthesis of the $BaFe_{12}O_{19}$@MoS_2 core-shell composite. This growth process is affected by various factors, including thiourea composition, temperature, sample thickness, and the duration of the hydrothermal synthesis.

Hydrothermal synthesis prepares a path for the growth of MoS_2 nanoflowers on the surface of $BaFe_{12}O_{19}$.

The concentration of thiourea directly influences the growth of the MoS_2 core-shell in the $BaFe_{12}O_{19}$@MoS_2 composite. As the thiourea composition increases, there is a corresponding increase in the growth of the MoS_2 core-shell. Consequently, the $BaFe_{12}O_{19}$@MoS_2 core-shell composite exhibits a higher tendency to absorb electromagnetic wave absorption to its maximum capacity.

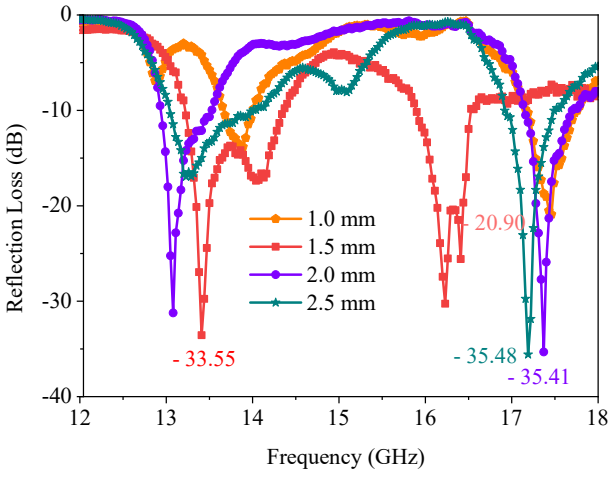

Fig. 15. Reflection loss of the $BaFe_{12}O_{19}$@MoS_2 core-shell composites (C_{10}) at various sample thicknesses

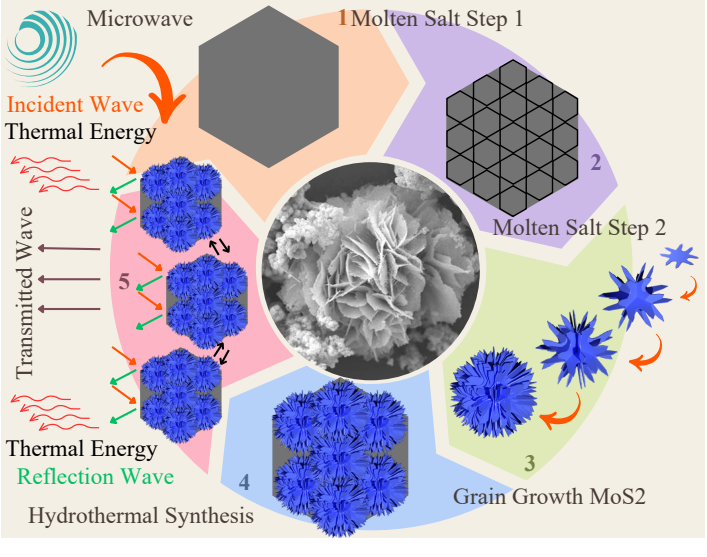

Fig. 16. Mechanism of MoS_2 nanoflower growth on $BaFe_{12}O_{19}$ in the $BaFe_{12}O_{19}$@MoS_2 core-shell composite

Table 6

Summary of recent findings on composites with a ferrite matrix or molybdenum as reinforcement decreases the ability to reflect an electromagnetic wave

Material	RL (dB)	Frequency (GHz)	Thickness (mm)	Reference
CF@MoS_2	−21.4	10.85	3.8	[32]
2–0 MoS_2 Ni NPs	−19.7	16.44	2.92	[33]
MoS_2@$Ti_3C_2T_x$	−51.0	6.1	4.0	[34]
MoS_2@AC	−31.8	16.72	7.0	[35]
Fe_3O_4@Fe	−30.5	6.2	2.0	[36]
$BaFe_{12}O_{19}$@CaF_2O_4	−36.8	9.9	2.9	[37]
$BaFe_{12x-2x}(Mn_{0.5}Co_{0.5}Ti)_xO_{19}$	−40.2	14.9	2.3	[38]
$BaFe_{12}O_{19}$@MoS_2	−35.41	17.37	2.0	This study

6. Discussion of the investigation results of $BaFe_{12}O_{19}$@MoS_2 core-shell composite by controlling hydrothermal parameters

The study began by observing that the $BaFe_{12}O_{19}$@MoS_2 core-shell composite single phase has appropriately been synthesized from the alloy of its raw materials, as shown in Fig. 2 and enhanced by refinement using the Material Analysis Using Diffraction (MAUD) software to make the observed pattern match the calculated ones shown in Table 2. Refinement findings were allowed if they fulfilled the R-weighted profile (Rwp), R-expected profile (Rexp), and SIG reliability index. The SIG parameter in the MAUD programme is used to assess how well crystal structure models generated from x-ray diffraction patterns corresponded to actuality. This metric assesses the similarity of observed and calculated diffraction patterns. During refinement, parameter values are expected to fluctuate. The higher the agreement between observed and calculated diffraction patterns, the lower the accuracy index. The efficiency of the refinement in this inquiry is proved by its compliance with the accuracy constraints of SIG 4, Rwp 20 %, and Rexp 15 %, as evidenced in Table 2. The EDS mapping in Fig. 3 is confirmed to have a successfully homogeneous distribution. Since the composite is a nonconductive material, the samples will be coated with gold. Therefore, Fig. 4 confirms the detection of gold as a coating during the sample preparation. The presented composition of element mapping is confirmed in Table 3. The absorption of electromagnetic waves in anti-radar composite materials is associated with the morphological shape of the composite surface. As seen in Fig. 5, 7, the morphological formation of nanoflowers using SEM proved effective in absorbing electromagnetic waves. This study also observed the effect of increasing the composition of thiourea in composites. Increasing the composition of thiourea will increase $BaFe_{12}O_{19}$@MoS_2 particle size, as shown in Fig. 6, and the effect will improve the absorption of electromagnetic waves. As shown in Fig. 8–10, in the composite process, the composition of thiourea, temperature, and holding time can all impact the particle size distribution. Fig. 5 confirms that $BaFe_{12}O_{19}$ has a hexagonal, plate-like structure. MoS_2, on the other hand, tends to generate spherical nanoflowers even though the XRD characterization shows that they both have the same crystal structure, namely hexagonal. PSA can form spherical particles even though BHF has a hexagonal crystal structure because of differences in particle size between PSA and SEM characterization, as shown in Tables 4, 5. Simultaneously, it is essential to note that SEM analysis is subject to a limitation on the spectrum point, representing the whole surface of the sample. The intensity of light diffused on the particles in the suspension is used to determine particle size. According to dynamic light scattering (DLS), when dispersed particles are exposed to a monochromatic ray, the intensity of light dispersing on fluctuating moving particles depends on the diffusion coefficient [32–39]. The slower movement of larger particles leads to a slower fluctuation in the emitted light intensity, while smaller particles exhibit quick fluctuations, resulting in intensity oscillations. The oscillation frequency calculates the diffusion coefficient depending on the particle size [40].

According to a study [41], the addition of Mo dope caused a decrease in the values of *Ms*, *Mr*, and *Hc* when compared to the untreated samples, as shown in Fig. 11. By looking at the thiourea composition (Fig. 12), temperature (Fig. 13), hydrothermal holding time (Fig. 14), and sample thickness (Fig. 15), the study was able to find different ways to reduce the reflection loss. An increase in hydrothermal temperature increases the number and growth of nanoflower cell nuclei, while an increase in hydrothermal holding time increases the density and depth of the nanoflower petals. The large MoS_2 nanoflower structure with tightly closed petals tends to produce maximum EM dissipation and scattering effects in core-cell composite systems. The hydrothermal temperature parameter has the most significant effectiveness in reducing reflection loss by 228.47 %, followed by the thiourea composition parameter with a reduction of reflection loss of 149.01 %, the sample thickness parameter with a reduction of reflection loss of 69.76 %, and the hydrothermal holding time parameter with a reduction of reflection loss of 58 %. Previous research has demonstrated that the hydrothermal temperature represents the essential synthesis parameter with the most significant impact [42].

As demonstrated in Table 6, this study produced the best candidate with an RL of –35.41 dB (17.37 GHz, Ku band) and 99.97 % absorption at the narrowest sample thickness of 2 mm. Several researchers have reported that a core-shell composite is a hierarchical structure that can improve RAM performance. Because of its dielectric properties, MoS_2 is becoming a more popular alternative because it may be used as a booster to modify polarization and reduce RL.

The study used a two-step molten salt synthesis approach, with a subsequent focus on the ongoing control of hydrothermal conditions. The primary objective of the first stage in molten salt synthesis is to decrease the solid-state's temperature from around 1423 K [43] to 1373 °C, as seen in Fig. 16. In contrast, the second step, involving molten salt, attempts to enhance the surface pathway of $BaFe_{12}O_{19}$ in order to facilitate the growth pathway of MoS_2. Fig. 16 illustrates that EM waves that hit the sample have three characteristics: absorption, transmission, and reflection. The design of this study is to maximize absorption and minimal reflection of EM waves. The microwave absorption mechanism of $BaFe_{12}O_{19}$@MoS_2 core-shell composites is significantly complex and involves multiple stages. The magnetic and dielectric losses of the composite material reduce the microwave signal. Magnetic loss occurs due to $BaFe_{12}O_{19}$, which has high magnetic permeability and generates eddy currents in response to an applied electromagnetic field [44]. In addition, it is essential to note that $BaFe_{12}O_{19}$ exhibits significant magneto-crystalline anisotropy, resulting in considerable reflection loss [45]. Moreover, the dielectric loss can be attributed to MoS_2 nanoflowers, characterized by a high dielectric constant and the ability to store energy inside an electric field [46, 47]. Dielectric loss occurs when a pulse of electromagnetic radiation passes through a material and causes the molecules inside the material to polarize. Polarization causes thermal effects, which result in energy dissipation and a reduction in the strength of the electromagnetic wave [18, 19]. In an external electromagnetic field, the delay of dipoles turning around would consume the incident microwave [44]. The mechanisms present include assistant eddy current, magnetic resonance loss, enhanced impedance matching, dielectric loss, multiple reflection and scattering effects, and interface polarization loss [47], all contributing to reducing the microwave signal further and improving the material's absorption performance.

This study's limitation is a challenging improvement due to the non-uniform size of the $BaFe_{12}O_{19}$@MoS_2 particle, which resulted in a PDI value in the range of 0.3–0.7.

It is essential to work with solid-state and hydrothermal temperatures. The following study must strictly control the different temperatures between the furnace display and $BaFe_{12}O_{19}$@MoS_2, which is critical to using a thermocouple. Further development of this research is measuring anti-radar performance at frequencies lower than 12 GHz to make an anti-radar more widely used in line with improved lifestyles and technological developments.

7. Conclusions

1. Incorporating MoS_2 into the C_{10} composition effectively protects the material from electromagnetic wave radiation, showing the potential to block radar signals. MoS_2 successfully covered $BaFe_{12}O_{19}$ and exhibited a uniform hexagonal shape evenly distributed on the surface. As seen in the T_{22}/H_{18} sample, the $BaFe_{12}O_{19}$@MoS_2 core-shell composite grows steadily, creating a nanoflower shape. This nanoflower shape represents the development of targeted modifications. It can absorb all incident waves to their fullest extent, significantly reducing both transmitted and reflected waves. This study successfully achieved the single-phase crystal structure of a $BaFe_{12}O_{19}$@MoS_2 core-shell composite. In this investigation, the composite system did not affect the crystal systems of its constituent compounds. The modification of the core-shell composite tends to follow the properties of $BaFe_{12}O_{19}$ as the core, demonstrating little change in the lattice parameters, the volume of the unit cell, and density.

2. The hydrothermal temperature contributes most crucially to controlling the morphology of the core-shell composite. Hydrothermal temperature control above 200 °C effectively prevents the emergence of nanorods that inhibit the absorption process of electromagnetic waves. Increased thiourea composition, temperature, and hydrothermal durability increase particle size. The core-shell composite nanoflower particle size increases with the petals' enhanced quantity and thickness to reduce reflection loss through scattering and dissipation effects. The growth and development of core-shell MoS_2 nanoflowers are affected by increasing hydrothermal temperature.

3. The investigation's findings demonstrated that the MoS_2 composition was the only factor influencing the magnetic properties of the $BaFe_{12}O_{19}$@MoS_2 core-shell composite. The increased MoS_2-composition of the $BaFe_{12}O_{19}$ succeeded in changing the hard magnet properties into soft magnets, which were the condition of the absorber materials.

4. A core-shell composite of $BaFe_{12}O_{19}$@MoS_2 demonstrated anti-radar capability with a low reflection loss of –35.41 at a temperature of 220 °C and a holding time of 18 hours. The remarkable of this study is that obtaining the thinnest sample thickness of 2 mm can result in microwave absorption of up to 99.97 % at a frequency of 17.37 GHz. The hydrothermal temperature is a crucial process parameter that has played an essential part in reducing reflection loss up to 228.47 %.

Conflict of interest

The authors declare that they have no conflict of interest concerning this research, whether financial, personal, authorship or otherwise, that could affect the research and its results presented in this paper.

Financing

The Ministry of Education, Culture, Research, and Technology of the Republic of Indonesia funded this project through the PDI grant with contract B/248/UN43.9/PT.01.03/2023.

Data availability

Data will be made available on reasonable request.

Use of artificial intelligence

The authors confirm that they did not use artificial intelligence technologies when creating the current work.

References

1. Asghar, G., Asri, S., Khusro, S. N., Tariq, G. H., Awan, M. S., Irshad, M., Safeen, A. et al. (2020). Enhanced Magnetic Properties of Barium Hexaferrite. Journal of Electronic Materials, 49 (7), 4318–4323. doi: https://doi.org/10.1007/s11664-020-08125-7
2. Hema, S., Sambhudevan, S. (2021). Ferrite-based polymer nanocomposites as shielding materials: a review. Chemical Papers, 75 (8), 3697–3710. doi: https://doi.org/10.1007/s11696-021-01664-1
3. Nikmanesh, H., Hoghoghifard, S., Hadi-Sichani, B., Moradi, M. (2020). Erbium-chromium substituted strontium hexaferrite particles: Characterization of the physical and Ku-band microwave absorption properties. Materials Science and Engineering: B, 262, 114796. doi: https://doi.org/10.1016/j.mseb.2020.114796
4. Yustanti, E., Trenggono, A., Manaf, A. (2020). Physical and Microwave Absorption Characteristics of High Powered Ultrasonically Irradiated Crystalline $BaFe_9Mn_{1.5}Ti_{1.5}O_{19}$ Particles. International Journal of Technology, 11 (2), 310. doi: https://doi.org/10.14716/ijtech.v11i2.2988
5. Feng, G., Zhou, W., Deng, H., Chen, D., Qing, Y., Wang, C. et al. (2019). Co substituted $BaFe_{12}O_{19}$ ceramics with enhanced magnetic resonance behavior and microwave absorption properties in 2.6 – 18 GHz. Ceramics International, 45 (11), 13859–13864. doi: https://doi.org/10.1016/j.ceramint.2019.04.083
6. Yang, E., Qi, X., Xie, R., Bai, Z., Jiang, Y., Qin, S. et al. (2018). Core@shell@shell structured carbon-based magnetic ternary nanohybrids: Synthesis and their enhanced microwave absorption properties. Applied Surface Science, 441, 780–790. doi: https://doi.org/10.1016/j.apsusc.2018.02.029
7. Wang, M., Lin, Y., Yang, H., Qiu, Y., Wang, S. (2020). A novel plate-like $BaFe_{12}O_{19}$@MoS_2 core-shell structure composite with excellent microwave absorbing properties. Journal of Alloys and Compounds, 817, 153265. doi: https://doi.org/10.1016/j.jallcom.2019.153265

8. Rianna, M., Sembiring, T., Situmorang, M., Kurniawan, C., Tetuko, A. P., Setiadi, E. A. et al. (2019). Effect of calcination temperature on Microstructures, magnetic properties, and microwave absorption on $BaFe_{11.6}Mg_{0.2}Al_{0.2}O_{19}$ synthesized from natural iron sand. Case Studies in Thermal Engineering, 13, 100393. doi: https://doi.org/10.1016/j.csite.2019.100393
9. Zhang, Y., Gao, S., Xing, H. (2019). Hierarchical core–shell Fe_3O_4@C@MoS_2 composites synergistically enhance microwave absorption. Materials Letters, 246, 80–83. doi: https://doi.org/10.1016/j.matlet.2019.03.031
10. Wang, P., Zhang, J., Wang, G., Duan, B., He, D., Wang, T., Li, F. (2019). Synthesis and characterization of MoS_2/Fe@Fe_3O_4 nanocomposites exhibiting enhanced microwave absorption performance at normal and oblique incidences. Journal of Materials Science & Technology, 35 (9), 1931–1939. doi: https://doi.org/10.1016/j.jmst.2019.05.021
11. Zhang, D., Chai, J., Cheng, J., Jia, Y., Yang, X., Wang, H. et al. (2018). Highly efficient microwave absorption properties and broadened absorption bandwidth of MoS_2-iron oxide hybrids and MoS_2-based reduced graphene oxide hybrids with Hetero-structures. Applied Surface Science, 462, 872–882. doi: https://doi.org/10.1016/j.apsusc.2018.08.152
12. Almessiere, M. A., Slimani, Y., Korkmaz, A. D., Baykal, A., Güngüneş, H., Sözeri, H. et al. (2019). Impact of La^{3+} and Y^{3+} ion substitutions on structural, magnetic and microwave properties of $Ni_{0.3}Cu_{0.3}Zn_{0.4}Fe_2O_4$ nanospinel ferrites synthesized via sonochemical route. RSC Advances, 9 (53), 30671–30684. doi: https://doi.org/10.1039/c9ra06353f
13. Huang, W., Tong, Z., Bi, Y., Ma, M., Liao, Z., Wu, G. et al. (2021). Synthesis and microwave absorption properties of coralloid core-shell structure NiS/Ni_3S_4@PPy@MoS_2 nanowires. Journal of Colloid and Interface Science, 599, 262–270. doi: https://doi.org/10.1016/j.jcis.2021.04.107
14. Yang, H., Zhang, X., Xiong, Z., Shen, Z., Liu, C., Xie, Y. (2021). Cu_2O@nanoporous carbon composites derived from Cu-based MOFs with ultrabroad-bandwidth electromagnetic wave absorbing performance. Ceramics International, 47 (2), 2155–2164. doi: https://doi.org/10.1016/j.ceramint.2020.09.053
15. Dai, B., Ma, Y., Dong, F., Yu, J., Ma, M., Thabet, H. K. et al. (2022). Overview of MXene and conducting polymer matrix composites for electromagnetic wave absorption. Advanced Composites and Hybrid Materials, 5 (2), 704–754. doi: https://doi.org/10.1007/s42114-022-00510-6
16. Karim Darboe, A., Qi, X., Gong, X., Peng, Q., Chen, Y., Xie, R. et al. (2022). Constructing $MoSe_2$/MoS_2 and MoS_2/$MoSe_2$ inner and outer-interchangeable flower-like heterojunctions: A combined strategy of interface polarization and morphology configuration to optimize microwave absorption performance. Journal of Colloid and Interface Science, 624, 204–218. doi: https://doi.org/10.1016/j.jcis.2022.05.078
17. Chang, M., Jia, Z., Wu, G., Yin, P. (2023). Multiple dimension-component designed Co/Co_9S_8/$Ti_3C_2T_x$ MXene composite for enhanced microwave absorption. Applied Physics Letters, 122 (13). doi: https://doi.org/10.1063/5.0142497
18. Hou, T., Wang, J., Zheng, T., Liu, Y., Wu, G., Yin, P. (2023). Anion Exchange of Metal Particles on Carbon-Based Skeletons for Promoting Dielectric Equilibrium and High-Efficiency Electromagnetic Wave Absorption. Small, 19 (42). doi: https://doi.org/10.1002/smll.202303463
19. Zheng, T., Zhang, Y., Jia, Z., Zhu, J., Wu, G., Yin, P. (2023). Customized dielectric-magnetic balance enhanced electromagnetic wave absorption performance in Cu_xS/$CoFe_2O_4$ composites. Chemical Engineering Journal, 457, 140876. doi: https://doi.org/10.1016/j.cej.2022.140876
20. Wang, S., Gao, H., Sun, G., Zhang, J., Xia, Y., Xie, C. et al. (2020). M-type Barium Hexaferrite Nanoparticles Synthesized by γ-Ray Irradiation Assisted Polyacrylamide Gel Method and Its Optical, Magnetic and Supercapacitive Performances. Journal of Cluster Science, 32 (3), 569–578. doi: https://doi.org/10.1007/s10876-020-01815-6
21. Maswadeh, Y., Mahmood, S. H., Awadallah, A., Aloqaily, A. N. (2015). Synthesis and structural characterization of nonstoichiometric barium hexaferrite materials with Fe:Ba ratio of 11.5 – 16.16. IOP Conference Series: Materials Science and Engineering, 92, 012019. doi: https://doi.org/10.1088/1757-899x/92/1/012019
22. Quilty, C. D., Housel, L. M., Bock, D. C., Dunkin, M. R., Wang, L., Lutz, D. M. et al. (2019). Ex Situ and Operando XRD and XAS Analysis of MoS_2: A Lithiation Study of Bulk and Nanosheet Materials. ACS Applied Energy Materials, 2 (10), 7635–7646. doi: https://doi.org/10.1021/acsaem.9b01538
23. Albiter, M. A., Huirache-Acuña, R., Paraguay-Delgado, F., Rico, J. L., Alonso-Nuñez, G. (2006). Synthesis of MoS_2 nanorods and their catalytic test in the HDS of dibenzothiophene. Nanotechnology, 17 (14), 3473–3481. doi: https://doi.org/10.1088/0957-4484/17/14/020
24. Sulaiman, N. I., Abu Bakar, M., Abu Bakar, N. H. H., Saito, N., Thai, V.-P. (2023). Modified sol–gel method for synthesis and structure characterisation of ternary and quaternary ferrite-based oxides for thermogravimetrically carbon dioxide adsorption. Chemical Papers, 77 (6), 3051–3074. doi: https://doi.org/10.1007/s11696-023-02687-6
25. Hu, F., Nan, H., Wang, M., Lin, Y., Yang, H., Qiu, Y., Wen, B. (2021). Construction of core-shell $BaFe_{12}O_{19}$@MnO_2 composite for effectively enhancing microwave absorption performance. Ceramics International, 47 (12), 16579–16587. doi: https://doi.org/10.1016/j.ceramint.2021.02.229
26. Lu, C.-H., Yeh, C.-H. (2000). Influence of hydrothermal conditions on the morphology and particle size of zinc oxide powder. Ceramics International, 26 (4), 351–357. doi: https://doi.org/10.1016/s0272-8842(99)00063-2
27. Goel, S., Garg, A., Gupta, R. K., Dubey, A., Prasad, N. E., Tyagi, S. (2020). Development of RGO/$BaFe_{12}O_{19}$-based composite medium for improved microwave absorption applications. Applied Physics A, 126 (6). doi: https://doi.org/10.1007/s00339-020-03613-3
28. Alshoaibi, A. (2023). Investigating the Supercapacitive Performance of Cobalt Sulfide Nanostructures Prepared Using a Hydrothermal Method. Materials, 16 (13). doi: https://doi.org/10.3390/ma16134512

29. Li, W., Shi, E., Fukuda, T. (2003). Particle size of powders under hydrothermal conditions. Crystal Research and Technology, 38 (10), 847–858. doi: https://doi.org/10.1002/crat.200310103
30. Zhai, Y., Zhu, D., Zhou, W., Min, D., Luo, F. (2018). Enhanced impedance matching and microwave absorption properties of the MAMs by using ball-milled flaky carbonyl iron-BaFe12O19 as compound absorbent. Journal of Magnetism and Magnetic Materials, 467, 82–88. doi: https://doi.org/10.1016/j.jmmm.2018.07.031
31. Ari Adi, W., Sarwanto, Y., Taryana, Y., Soegijono, B. (2018). Effects of the geometry factor on the reflection loss characteristics of the modified lanthanum manganite. Journal of Physics: Conference Series, 1091, 012028. doi: https://doi.org/10.1088/1742-6596/1091/1/012028
32. Zhang, W., Zhang, X., Zhu, Q., Zheng, Y., Liotta, L. F., Wu, H. (2021). High-efficiency and wide-bandwidth microwave absorbers based on MoS_2-coated carbon fiber. Journal of Colloid and Interface Science, 586, 457–468. doi: https://doi.org/10.1016/j.jcis.2020.10.109
33. Sun, Y., Zhong, W., Wang, Y., Xu, X., Wang, T., Wu, L., Du, Y. (2017). MoS2-Based Mixed-Dimensional van der Waals Heterostructures: A New Platform for Excellent and Controllable Microwave-Absorption Performance. ACS Applied Materials & Interfaces, 9 (39), 34243–34255. doi: https://doi.org/10.1021/acsami.7b10114
34. Hassan, A., Aslam, M. A., Bilal, M., Khan, M. S., ur Rehman, S., Ma, K. et al. (2021). Modulating dielectric loss of MoS_2@$Ti_3C_2T_x$ nanoarchitectures for electromagnetic wave absorption with radar cross section reduction performance verified through simulations. Ceramics International, 47 (14), 20706–20716. doi: https://doi.org/10.1016/j.ceramint.2021.04.014
35. Negi, P., Kumar, A. (2021). MoS_2 nanoparticle/activated carbon composite as a dual-band material for absorbing microwaves. Nanoscale Advances, 3 (14), 4196–4206. doi: https://doi.org/10.1039/d1na00292a
36. Qu, B., Zhu, C., Li, C., Zhang, X., Chen, Y. (2016). Coupling Hollow Fe_3O_4–Fe Nanoparticles with Graphene Sheets for High-Performance Electromagnetic Wave Absorbing Material. ACS Applied Materials & Interfaces, 8 (6), 3730–3735. doi: https://doi.org/10.1021/acsami.5b12789
37. Lin, Y., Liu, X., Ye, T., Yang, H., Wang, F., Liu, C. (2016). Synthesis and characterization of graphene/$0.8BaFe_{12}O_{19}$/$0.2Y_3Fe_5O_{12}$ nanocomposite. Journal of Alloys and Compounds, 683, 559–566. doi: https://doi.org/10.1016/j.jallcom.2016.05.117
38. Li, H., Zheng, L., Deng, D., Yi, X., Zhang, X., Luo, X. et al. (2021). Multiple natural resonances broaden microwave absorption bandwidth of substituted M-type hexaferrites. Journal of Alloys and Compounds, 862, 158638. doi: https://doi.org/10.1016/j.jallcom.2021.158638
39. McComiskey, K. P. M., Tajber, L. (2018). Comparison of particle size methodology and assessment of nanoparticle tracking analysis (NTA) as a tool for live monitoring of crystallisation pathways. European Journal of Pharmaceutics and Biopharmaceutics, 130, 314–326. doi: https://doi.org/10.1016/j.ejpb.2018.07.012
40. Jose, N., Deshmukh, G. P., Ravindra, M. R. (2019). Dynamic Light Scattering: Advantages and Applications. Acta Scientific Nutritional Health, 3 (3), 50–52. Available at: https://www.actascientific.com/ASNH/pdf/ASNH-03-0194.pdf
41. Almessiere, M. A., Güner, S., Slimani, Y., Korkmaz, A. D., Baykal, A. (2022). Effect of Mo substitution on structure, morphology and magnetic features of $Sr_{0.8}Ni_{0.2}Fe_{12-2x}Mo_xO_{19}$ ($x \leq 0.35$) hexaferrites. Chemical Papers, 77 (2), 947–956. doi: https://doi.org/10.1007/s11696-022-02527-z
42. Yustanti, E., Noviyanto, A., Ikramullah, M., Marsillam, Y. A., Taryana, Y., Taufiq, A. (2023). High-performance microwave absorption by optimizing hydrothermal synthesis of $BaFe_{12}O_{19}$@MnO_2 core–shell composites. RSC Advances, 13 (39), 27634–27647. doi: https://doi.org/10.1039/d3ra05114e
43. Liu, D., Liu, H., Ning, S., Chu, Y. (2020). Chrysanthemum-like high-entropy diboride nanoflowers: A new class of high-entropy nanomaterials. Journal of Advanced Ceramics, 9 (3), 339–348. doi: https://doi.org/10.1007/s40145-020-0373-x
44. Yin, P., Wu, G., Tang, Y., Liu, S., Zhang, Y., Bu, G. et al. (2022). Structure regulation in N-doping biconical carbon frame decorated with $CoFe_2O_4$ and (Fe,Ni) for broadband microwave absorption. Chemical Engineering Journal, 446, 136975. doi: https://doi.org/10.1016/j.cej.2022.136975
45. Khan, M. Z., Gul, I. H., Javaid, F., Ali, A., Hafeez, S., Baig, M. M. (2023). Synthesis and Characterization of Zr^{4+}-Y^{3+} Substituted Ba-Sr Hexaferrite Nanoparticles for Microwave Absorption and Electromagnetic Shielding Applications. Materials Research Bulletin, 168, 112468. doi: https://doi.org/10.1016/j.materresbull.2023.112468
46. Sparavigna, A. C. (2023). Iron Oxide Fe_3O_4 Nanoparticles with ICPs and Biochar to Improve Electromagnetic Shielding Performance. SSRN Electronic Journal. doi: https://doi.org/10.2139/ssrn.4331866
47. Luo, Y., Yin, P., Wu, G., Zhang, L., Ma, G., Wang, J. et al. (2022). Porous carbon sphere decorated with Co/Ni nanoparticles for strong and broadband electromagnetic dissipation. Carbon, 197, 389–399. doi: https://doi.org/10.1016/j.carbon.2022.06.084